Iran University of Science and Technology

Automotive Science and Engineering

Journal Homepage: ase.iust.ac.ir

ISSN: 2008-9899

Experimental Data-Based Machine Learning Prediction of Crashworthiness Parameters and Energy Absorption

Iman Nejati Ajibisheh [1], Javad Rezapour[1*], Sina Gohari Rad[2]

[1] Department of Mechanical Engineering, La.C, Islamic Azad University, Lahijan, Iran,

[2] Department of Mechanical Engineering, Ra.C, Islamic Azad University, Rasht, Iran,

ARTICLE INFO

Article history:

Received : 14 Dec 2025

Accepted: 16 Mar 2026

Published: 29 Mar 2026

Keywords:

Artificial neural network

Machine learning

Crashworthiness

Force-time response

high velocity impact

A B S T R A C T

Thin-walled tubes are effective crashworthiness structures that absorb energy under axial loading, while preventing the transmission of injurious acceleration and excessive forces to the protected section and thereby reducing damage severity. This study presents a high-accuracy artificial neural network (ANN) framework for predicting the dynamic response and impact resistance of thin-walled steel tubes under high-velocity axial impacts. The model was developed using a hybrid dataset comprising 300 experimental impact tests and 4000 finite element (FE) simulations, with systematic variations in tube geometry and impact conditions. After parameter optimization, the final model consisted of a 24-layer network with 180 neurons per layer and achieved high accuracy (R-value above 0.985). Error assessments across the four physical criteria (PFE, MFE, AEE, and SHE) show that the ANN predicts peak force, mean force, absorbed energy, and shortening with average errors generally below 10%, demonstrating strong predictive capability. Overall, the model not only offers a much faster alternative to FE simulations but also accurately reproduces oscillatory behavior and deformation progression, making it a reliable tool for impact response prediction.

1.Introduction

Thin-walled structures are extensively employed in engineering applications because of their remarkable ability to dissipate impact energy efficiently [1]. Their use is particularly widespread in the automotive and transportation sectors [2, 3], as well as in aerospace [4] and marine engineering [5]. The effectiveness of these components in crash and impact scenarios mainly arises from their capability to transform kinetic energy into plastic deformation during loading [5]. In addition to this superior energy-dissipation performance, their relatively low manufacturing and design costs have encouraged extensive research on their response under axial compression and impact conditions [6–13]. A considerable number of investigations have examined how the cross-sectional configuration and geometric features of thin-walled tubes influence their crashworthiness and energy-absorption performance under axial impact [14–18]. For example, Karagiozova and Jones [19] carried out a detailed analysis of thin-walled shells subjected to axial impact in order to clarify the buckling mechanism and its evolution. Their findings indicated that the buckling process is strongly affected by the impactor mass, impact velocity, and shell

*Corresponding Author
Email Address: javad.rezapour@iau.ac.ir
https://doi.org/10.22068/ase.2026.745

geometry. Xu et al. [20] employed a mathematical formulation in symplectic space to identify critical buckling loads and subsequent buckling modes under dynamic axial loading. In another study, Yamazaki and Han [21] proposed a method aimed at improving and maximizing the crashworthiness of thin-walled cylindrical shells.

Sadeghi et al. [22] analytically and experimentally studied the effect of axial impact on the symmetric buckling behavior of strain-rate-sensitive thin-walled shells. Their work also assessed how strain hardening and strain-rate dependency influence shell shortening, buckling pattern, and axial reaction force. Sun et al. [23] introduced an analytical model based on wave propagation theory to investigate the dynamic buckling of cylindrical shells under axial impact, concluding that buckling initiates at the impacted end when the traveling wave is not reflected. Yao et al. [24] numerically evaluated the role of geometric variables in the energy-absorption behavior of conventional corrugated tubes (OCT) and hybrid corrugated tubes (HCT). Their results demonstrated that HCTs exhibit superior energy-absorption characteristics compared with OCTs. They further showed that the wavelength and fixed corrugation ratio significantly affect both the deformation mechanism and the crashworthiness indicators of HCTs. Ferdynus et al. [25] explored, through experiments and numerical modeling, the crashworthiness and energy-absorption performance of dented square columns under axial impact, identifying the most effective dent geometry and location. Feli et al. [26] analyzed grooved conical thin-walled tubes subjected to impact loading by proposing a novel analytical model and validating it against numerical results. Their study focused on the influence of several geometric variables, such as groove number, wall thickness, and thickness gradient, on crushing behavior and absorbed energy in comparison with conventional conical tubes. Jamal-Omidi and Choopanian Benis [27] numerically investigated the crashworthiness and energy-absorption capability of laterally corrugated composite tubes under axial loads, paying particular attention to the role of wave amplitude and the number of corrugation waves in altering cross-sectional form. Lu et al. [28] examined square-circle hybrid section (SCHS) tubes under axial compression using finite element simulations. They evaluated the influence of geometric design variables, including the placement of connecting plates and the dimensional relationship between the circular and square parts, on crashworthiness behavior. Khalkhali et al. [29] proposed a predictive model for the crashworthiness parameters of composite cylindrical tubes. Using data obtained from finite element simulations, they developed two meta-models capable of estimating the absorbed energy and the maximum crushing force based on the geometric design variables.

Bhutada and Goel [30] also provided a comprehensive review of tube crushing mechanisms and crashworthiness performance under axial impact, highlighting the significance of geometric modification and filler materials in improving force-displacement response.

As suggested by these studies, understanding the influence of geometry on the energy-absorption characteristics and crashworthiness of thin-walled members remains an important topic in this field. Nevertheless, experimental investigations of all possible configurations are costly and impractical, while numerical simulations often demand substantial computational time. Furthermore, because analytical solutions become increasingly difficult to apply in strongly nonlinear impact problems, recent research has increasingly turned toward machine learning techniques and artificial neural networks (ANNs) for modeling the behavior of thin-walled shells. Guarize et al. [31], for instance, adopted a hybrid ANN-FE framework to establish a nonlinear relationship between system inputs and outputs in random dynamic analysis, significantly reducing the required computational time. Their results indicated that the response history could be obtained nearly twenty times faster than through conventional finite element simulation. Mandal [32] applied an ANN model to estimate the buckling load of axially compressed thin-walled shells using an extensive database of published experimental results, and the predicted loads were within 10% of the measured values.

[DOI: 10.22068/ase.2026.745]

Dastjerdi et al. [33] investigated the multi-objective optimization of double-walled cylindrical thin-walled structures with varying lengths under axial impact. In their work, absorbed energy and specific absorbed energy were treated as objective functions, while the maximum crushing force served as a design constraint. Their optimization process identified tube dimensions that maximize specific energy absorption while satisfying the allowable force limit. Chen et al. [34] carried out theoretical and multi-objective optimization studies on hybrid multicellular structures to obtain enhanced crashworthiness performance. By employing the normal boundary intersection method, they compared the optimized hybrid design with conventional multicellular structures of identical mass. Tahir et al. [35] also used ANN-based modeling to estimate the buckling load of thin-walled shells subjected to axial compression. Relying on nine input variables derived from experimental observations, they achieved predictions in close agreement with test data, with errors around 10%. Sakaridis et al. [36] proposed a machine-learning approach for forecasting the buckling response of tubular structures and assessing their sensitivity to initial imperfections. Their findings showed that the predictive accuracy of the model was comparable to the variation caused by minor geometric irregularities. In another study, Wang et al. [37] performed a multi-objective optimization to improve the crashworthiness of thin-walled energy absorbers filled with constant-thickness honeycomb cores. They also proposed a multi-criteria decision-making framework combining gray relational analysis with integrated entropy to determine an optimal trade-off between initial peak crushing force and absorbed energy along the Pareto frontier. Raouf et al. [38] investigated effect of the density of foam on the quasi-static loading response of foam filled and empty cylindrical tubes. They showed that when foam density increased by about two times, the peak load increased by 1%.

In this study, machine learning is employed to predict the crashworthiness characteristics and energy-absorption metrics of thin-walled shells subjected to high-velocity axial impact. A database of force-time responses is constructed using both experimental testing and finite element analysis by systematically varying key geometric parameters of the tubes, namely height, inner diameter, and wall thickness. In addition, loading conditions are defined by the striker mass and impact velocity. The resulting outputs include shortening, absorbed energy, first peak force, and mean crushing force. To model the nonlinear dynamic response of the structures, a feedforward artificial neural network is developed and trained. The results demonstrate that the trained network is capable of predicting impact behavior with high accuracy. Finally, the predictive performance of the model is evaluated using a separate test dataset and standard crashworthiness indicators.

1. Data Preparation

A dataset was assembled from both experiments and Abaqus/Explicit FE simulations to train and validate machine-learning models for predicting the force–time response of cylindrical tubes under axial impact. The inputs include tube height (60–105 mm), inner diameter (28–40 mm), thickness (1–2 mm), impact velocity (20–100 m/s), and striker mass (100–1000 g). Because experimental testing is limited, 300 cases were obtained experimentally and the remaining 4000 were generated numerically, yielding 4300 force–time curves covering a wide range of geometries and loading conditions.

2.1. Experimental Data

2.1.1. Material features

Table 1 presents the chemical analysis of the mild steel used in the experimental investigation.

Based on the ASTM E8, the static stress-strain curves of the utilized steel tubes were determined through STM machine (Figure 1). Figure 2 presents the steel specimens experimental stress-strain curves.

The yield stress is 291.9 MPa, and the elastic modulus, density, and Poisson ratio are obtained as 200 GPa, 7.864×10^{-6} Kg/mm3, and 0.30, respectively.

[DOI: 10.22068/ase.2026.745]

Table 1: Chemical composition of mild steel

Chemical Elements	Percentage
Fe	98.6356
C	0.1880
Al	0.0762
S	0.0342
Mn	0.8375
Ni	0.0217
Cr	0.0213
Si	0.1855

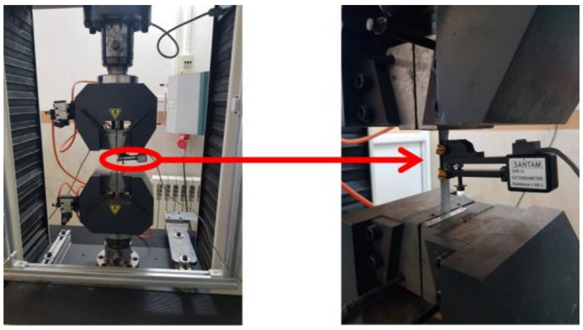

Figure 1: Tensile testing machine

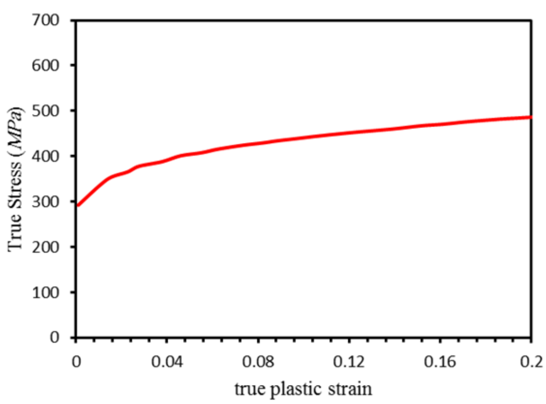

Figure 2: Quasi-static stress-strain curve

Figure 3: Experimental specimen sets of cylindrical tubes made of mild steel.

2.1.2. Sample Preparation Procedure

As shown in Figure 3, the cylindrical tubes are made of mild steel in 20 geometrical configurations. Table 2 presents the geometric characteristics of the cylindrical steel tubes mentioned.

2.1.3. Experimental setup

Empirical results for cylindrical steel tubes subjected to high-rate axial impact were obtained using a gas gun (Figure 4a). The force–time response was measured with a load cell (capacity:).

For each tube type listed in Table 2, axial impacts were conducted using three strikers with masses of 140, 262, and 360 g at five impact velocities (40, 60, 70, 80, and 100 m/s). This test matrix yielded 300 distinct force–time curves. To ensure repeatability, each test condition was performed three times and the results were averaged. A representative striker is shown in Figure 4b. All strikers had a length of 130 mm and a diameter of 45 mm, and the projectiles were made of VCN150 steel with an Ertalon coating. Examples of tube specimens mounted in the gas gun setup are presented in Figure 5.

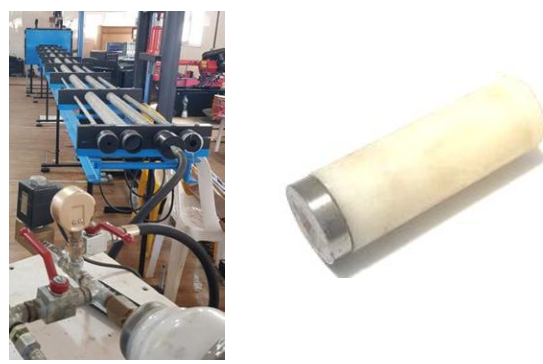

a b

Figure 4: (a) The gas gun that used in experimental tests. (b) one of the striking mass

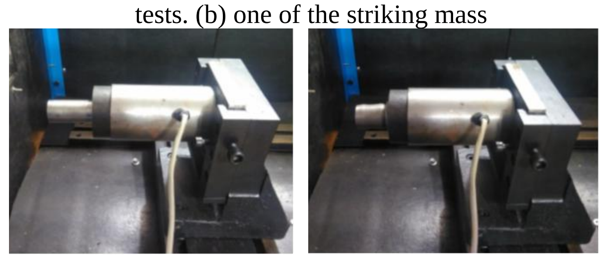

a b

Figure 5: (a) cylindrical steel tube before being impacted. (b) cylindrical steel tube after being impacted

[DOI: 10.22068/ase.2026.745]

Table 2: the geometric characteristics of the cylindrical steel tubes

Model Type	Thickness (mm)	Inner Diameter (mm)	Length (mm)	Mass (gr)
T1	1	30	104	79.7
T2	1	30	92	70.5
T3	1	30	82	62.8
T4	1	30	71	54.4
T5	1	30	61	46.7
T6	1	40	105	106.4
T7	1	40	100	101.3
T8	1	40	91	92.2
T9	1	40	81	82
T10	1	40	67	67.9
T11	2	29	102	156
T12	2	29	93	142.5
T13	2	29	83	127
T14	2	29	73	111.8
T15	2	29	65	99.6
T16	2	38	105	207.5
T17	2	38	90	177.9
T18	2	38	80	158
T19	2	38	68	134.4
T20	2	38	62	122.5

2.2. Numerical Simulations Data

Numerical simulations of the cylindrical tubes under axial impact were conducted using the commercial finite element (FE) software ABAQUS/Explicit. Following the previously mentioned criteria, 100 tube models were randomly generated by varying the length, inner diameter, and wall thickness within the ranges of 60–105 mm, 28–40 mm, and 1–2 mm, respectively. Each model was then simulated across 40 different impact scenarios. In total, 4,000 simulations were performed, with striker velocities and masses randomly and uniquely assigned within the ranges of 20–100 m/s and 100–1000 g, respectively.

To replicate experimental conditions, the tube was modeled with one end fixed to a rigid surface while the other was subjected to the striker's impact (Figure 6). The tubes were discretized using C3D8R elements with a 0.5 mm mesh size to ensure numerical convergence. A "general contact" algorithm was implemented to account for interactions between all surfaces.

Given the strain-rate sensitivity of mild steel, the Johnson–Cook constitutive model [39] was employed to define the dynamic flow behavior of the material as follows:

$$\sigma_d = (A + B(\varepsilon^p)^n)\left(1 + C\ln\left(\frac{\dot{\varepsilon}}{\dot{\varepsilon}^0}\right)\right) \tag{1}$$

Were A equal to the yield stress at reference strain rate, $\dot{\varepsilon}^0$ is a reference strain rate, and B, n, and C are material constants. Due to the similarity of the materials used in the current research and Sadeghi et al. [39], their obtained values of the Johnson-Cook constants used in simulations (table 3).

Table 3. the Johnson-Cook constants [37]

constant	A ($GPa \times 10^{-3}$)	B ($GPa \times 10^{-3}$)	n ($\times 10^{-3}$)	C ($\times 10^{-3}$)	$\dot{\varepsilon}^0$ ($1/s$) $\times 10^{-3}$
value	291.96	358.25	304.98	135.09	8.62

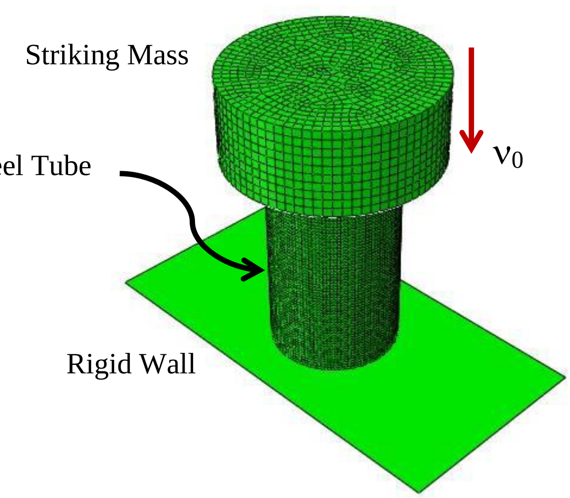

Figure 6: A view of assembled tube impacted by the striking mass in FE simulation

3. Machine learning algorithm

3.1. Principal concepts of ANNs

ANN is an example of an ML algorithm driven by the neural network function of the

[DOI: 10.22068/ase.2026.745]

human brain [40]. An ANN can be thought of as a nonlinear operator that captures an input vector A and returns the hypothesis value of the output vector B [41](Eq. 2):

$$B = ANN(A) \tag{2}$$

The ANN architecture considered in this paper is shown in Figure 7. The jth neuron in the Kth layer (F_j^K) shows the initiation of a linear combination of weights $w_{j,l}^K$ and basis b_j^K are network parameters and neurons from the prior layer F_l^{K-1} at time t_i. The activation function (f_{act}) can be the Rectified Linear Unit (ReLU), hyperbolic tangent (tanh), or sigmoid, as given in Eqs. (3a) and (3b):

$$\tau_j^K = \sum F_l^{K-1} w_{j,l}^K + b_j^K \tag{3.a}$$

$$F_j^K = f_{act}(\tau_j^K) \tag{3.b}$$

During training, network parameters in an ANN are updated to minimize error. Here, the error is the difference between the values predicted from the ANN with initialized network parameters and the real ones [39] and defined as Eq. (4):

$$Err = \frac{1}{2N} \sum_{m=1}^{N} (h_m - y_m)^2 \tag{4}$$

where Err denotes the error, N shows the sample number in the training set, h_m and y_m denote the hypothesized values from the ANN and the objective values of the mth output. The error can be minimized by using the optimization method.

3.2. ANN model architecture

ANN function f_{ANN} is considered for predicting the force history of a specific high velocity impact, which is defined to output a force value F_i as a time function t_i, the weight of striker mass M, the velocity of striker mass V_0, the length of tube L, the inner diameter of tube D_{In}, and the thickness of tube T_h,

$$f_{ANN} : \{t_i, M, V_0, L, D_{In}, T_h\} \rightarrow \{F_i\} \tag{5}$$

The tube displacement can then be obtained by estimating the acceleration history using the axial force history and the mass of the impacting striker. The ANN structure variations include an input layer with 6 input parameters mentioned above, hidden layers with a variable number ranging from 6 to 36, and an output layer that renders the force value. The hidden layers are fully connected. For activation function in the hidden layers, the ReLU and tanh functions are considered. The hidden layer size varies from 60 to 240 neurons per layer, with a 5% increase in the number of neurons.

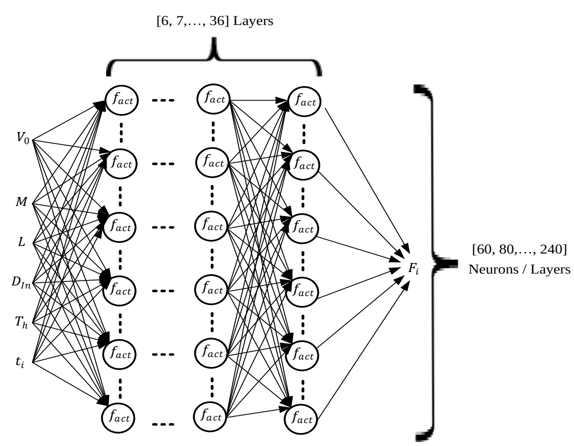

Figure 7: The ANN architecture with activation function

3.3. Embedding Mechanical Principles in the ANN Architecture

For an ANN model predicting, embedding physics and mechanics into the architecture is highly beneficial for generalization, stability, and data efficiency. The four mechanical principles of impact are implemented in the ANN architecture as follows.

[DOI: 10.22068/ase.2026.745]

3.3.1. Conservation of Momentum

At the onset of impact, the contact force is directly related to the rate of change of the striker's momentum as:

$$F_i(t) \approx \frac{d}{dt}(Mv) \tag{6}$$

The conservation of momentum is incorporated into the ANN architecture by introducing an additional penalty term into the cost function, thereby constraining the network predictions to remain consistent with the fundamental physical law:

$$\mathcal{L}_{mom} = \left\| \int F_i(t)dt - M(V_0 - V_f) \right\| \tag{7}$$

3.3.2. Conservation of Energy

The initial kinetic energy of the striker is given by:

$$E_k = \frac{1}{2} M {V_0}^2 \tag{8}$$

During the impact process, the initial kinetic energy of the striker is redistributed among several mechanisms, including irreversible plastic deformation of the tube, recoverable elastic strain energy, and various dissipative effects such as heat generation and stress wave propagation. This physical insight is incorporated by imposing a soft energy-based constraint within the learning framework in ANN architecture:

$$\int F_i(t)\delta(t)dt \leq \frac{1}{2} M {V_0}^2 \tag{9}$$

The network is constrained to avoid generating non-physical forces or predicting energy values that exceed the initial kinetic energy input, ensuring that all predictions remain consistent with fundamental physical principles.

3.3.3. Explicit Physical Constraints Imposed on the Network Outputs

To guarantee the physical consistency of the predicted impact response, a set of explicit physical constraints is imposed on the network outputs. The contact force is constrained to remain non-negative throughout the impact event, reflecting the compressive nature of the interaction between the striker and the tube. Additionally, the initial contact condition is enforced by requiring the contact force to vanish at the onset of impact. These physical constraints are expressed as follows:

$$\begin{aligned} 0 &\leq F_i(t) \\ 0 &= F_i(0) \end{aligned} \tag{10}$$

Moreover, the duration of contact is restricted to be finite and is formulated as a function of the striker mass and initial velocity, ensuring consistency with established principles of impact mechanics. Finally, non-physical oscillations and spurious high-frequency fluctuations in the predicted force–time histories are suppressed by applying temporal regularization strategies, which promote smoothness and enhance the physical realism of the model predictions.

3.3.4. Decomposition of the Force–Time Response into Physical Components

Rather than predicting the total force–time response directly, the impact force is represented as the superposition of distinct physically motivated components, corresponding to elastic, plastic, and inertial contributions. Within the proposed network architecture, each component is modeled and predicted independently, while the overall contact force is obtained through their linear aggregation.

$$\begin{aligned} F_i(t) = F_{elastic}(t) + F_{plastic}(t) \\ + F_{inertia}(t) \end{aligned} \tag{11}$$

This physically informed decomposition enhances the numerical stability of the learning

[DOI: 10.22068/ase.2026.745]

process and significantly improves the mechanical interpretability of the predicted force–time histories, enabling clearer insight into the dominant deformation and inertia mechanisms governing the impact response.

3.4. Dataset

Experimental and FE simulation results used to generate the data set were applied to train, test, and validate ANN models. To capture all deformation during the impact in output data, 1,000 points are selected from each force-time curve by setting the sampling step for the output result equal to $3 \times 10^{-7}\ s$. By considering the variables as high (h), inner diameter (D), and thickness (t_h) of tube, and the velocity (V_0) and mass (M_0) of striker, and force (F) and time (t_s) for output, the resulting dataset contains 4.3 million data points from 4,300 force-time curves. Data sets of 3,440, 473, and 387, or 80%, 11%, and 9% of force-time curves are used for training, testing, and validation, which are unknown data for the networks.

3.3. Training, testing, and validation method

The MATLAB Deep Learning Toolbox is employed for training and testing, and the feedforwardnet function is used to generate a multi-layer network that connects multiple inputs to a single output, with several neurons in each hidden layer. Bayesian regularization (trainbr) is used for training. This function updates bias and weight values using Levenberg-Marquardt optimization, minimizing the combined errors and weights to modify the linear combination of the network's parameters. Upon completion of training, the resulting network exhibits acceptable generalization [35]. The network's performance is good when the mean square error decreases with increasing iterations, and there is no significant discrepancy between the test and training errors. Network performance can be shown using regression plots of the test and training outputs. Finally, the ANN predictions are verified using the validation dataset.

4. Results

4.1. Results from experimental and finite element simulations

A total of 300 experimental tests are performed and a total of 4,000 simulations are conducted across 100 models and 40 loading scenarios, with most of the results used to train and test the ANN models. Figure 8 compares the force-time curves from experimental tests and numerical simulations. Moreover, the numerical and empirical buckling forms of the same sample models are shown in figure 9.

The numerical and experimental axial dislocations, i.e., the axial displacement of the striking mass, result in crushing of the impacted tube due to plastic deformation, peak forces, and energy absorption in some samples, as listed in Table 4.

Comparing the numerical simulation results with the experimental data demonstrates the high accuracy of the simulations, thereby validating their suitability for training and testing the ANN models.

Table 4. The experimental and numerical axial displacement, peak load and energy absorbing of T11 and T20

	Axial Displacement (mm)		Peak Load (kN)		Energy absorbing (J)	
Model	Exp.	Num.	Exp.	Num.	Exp.	Num.
T11	3.12	2.88	97.30	98.3	209.6	209.55
T20	8.1	7.93	112.89	114.37	647.99	647.98

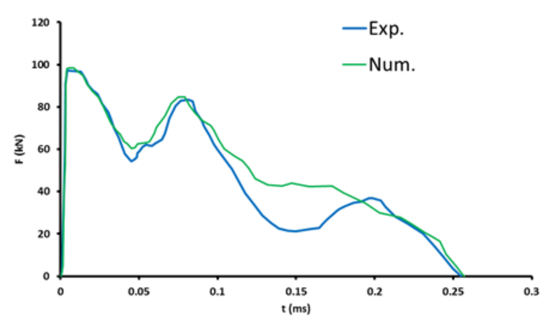

a)T11

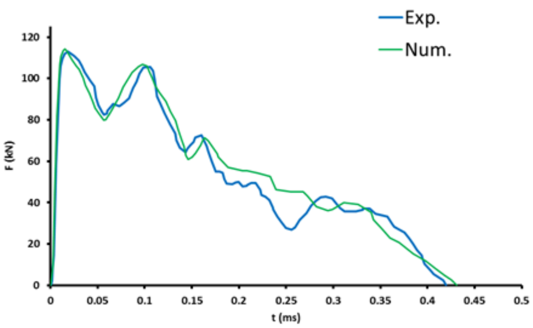

b)T20

Figure 8: The experimental and numerical force-time curves of a)T11 b)T20

4.2. Results from ANN modeling

The performance of the developed ANN models was initially evaluated by comparing various architectural configurations and analyzing their optimization trajectories. Following this, the calibrated model was rigorously assessed by comparing its predictions against finite element (FE) simulation results and experimental data concerning the impact behavior of the tubes.

Model	Exp. Buckling Shapes	Num. Buckling Shapes
T11)		
T20)		

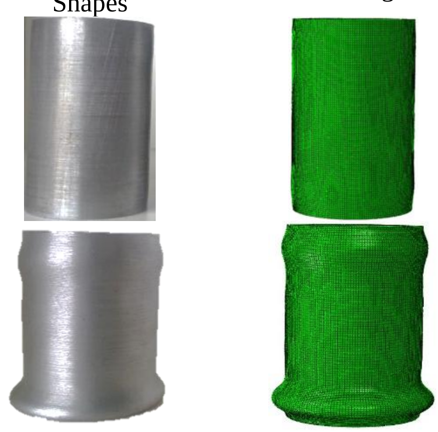

Figure 9: The experimental and numerical buckling shapes of the models T11 and T20

During the selection of the optimal network configuration, a balance between predictive accuracy and computational cost was maintained across training and validation sets. To account for stochastic variations during training, each architecture was trained three times. In the initial comparative analysis, the impact of the activation function and network depth (number of layers) was investigated. Four distinct experiments were performed, testing configurations with 60, 120, 180, and 240 neurons per layer. For each set, the depth was varied from 6 to 36 layers, utilizing both ReLU and tanh activation functions. The average validation losses are illustrated in Figure 10.

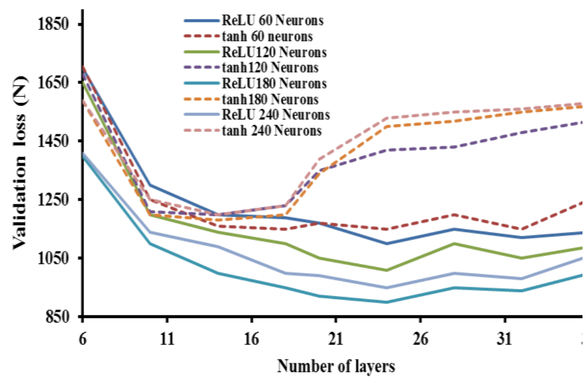

Figure 10: validation loss as a function of the number of hidden layers and activation functions

As shown in Figure 10 validation loss exhibits a downward trend with an increasing number of hidden layers when using the ReLU function. Conversely, the tanh function shows a different trend: once the number of hidden layers exceeds 20, validation loss begins to rise, an effect exacerbated by larger neuron counts. In general, it is observed that beyond a specific threshold (between 20 and 26 layers), increasing the depth yields diminishing returns and may even degrade performance. This threshold is contingent upon the activation function and layer size. Notably, the tanh function appears superior in shallower networks, whereas ReLU demonstrates better performance in deeper architectures.

Based on the model results, and in order to avoid an unnecessary increase in computational cost and network size while preserving strong predictive performance, a layer-size analysis was carried out using the ReLU activation function with 24 hidden layers. To identify the optimal layer size, the number of neurons per layer was varied from 60 to 240 in increments of

[DOI: 10.22068/ase.2026.745]

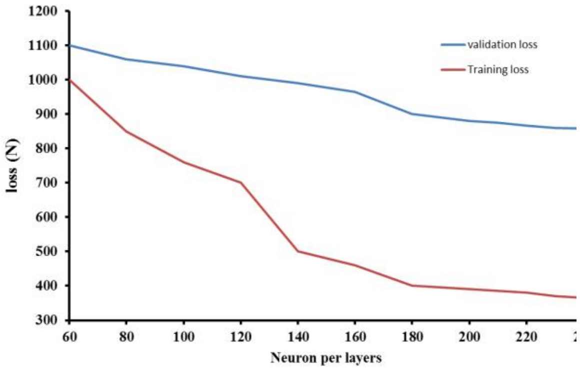

Figure 11: training and validation loss as a function of the number neurons per hidden layer

20. Figure 11 presents the corresponding training and validation loss trends.

As illustrated in the figure, model performance improves as the number of neurons in each layer increases. However, the gap between the training and validation losses also becomes larger with increasing neuron count. Therefore, architecture with 180 neurons per layer was selected as the optimal configuration for the model.

4.3. Evaluation of the Calibrated Model's Performance

Two common approaches for assessing ANN training performance are the mean squared error (MSE) and network training regression plots. The neural network's training performance is quantified using MSE, which measures the average squared difference between actual and predicted values. The relationship between the number of epochs and MSE illustrates how network performance evolves as training progresses. An epoch is defined as one complete pass of the learning algorithm through the entire training dataset. A well-performing network is characterized by a decreasing MSE with increasing epochs and minimal discrepancy between training and testing errors.

Figure 12 shows the variation in MSE with the number of epochs for both the training and test datasets. Ideally, the training and testing curves

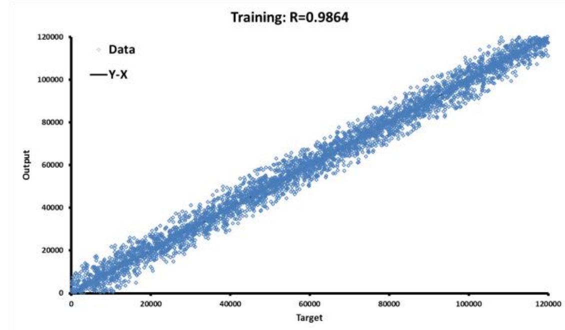

a)training

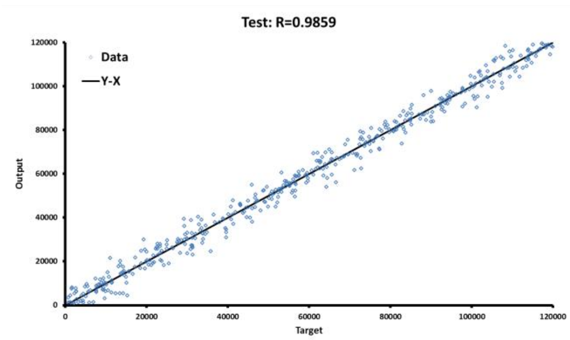

b)testing

Figure 13: Regression plots for the a)training and b)testing data outputs

should follow a similar trajectory, indicating optimal network training. In this study, the minimum error is obtained at 35 epochs. Beyond this point, the difference between training and testing errors becomes minimal and may be considered negligible as the number of iterations increases.

Network performance is evaluated using regression plots of the training and test data outputs with respect to the target values. The test set is used to assess the quality of the outcome, and it is not used at any stage of the prior process to determine the network architecture. A strong positive correlation between the network outputs and the targets is expected, with the data points distributed closely along the 1:1 line and the correlation coefficient (R-value) for both the training and test datasets approaching unity.

[DOI: 10.22068/ase.2026.745]

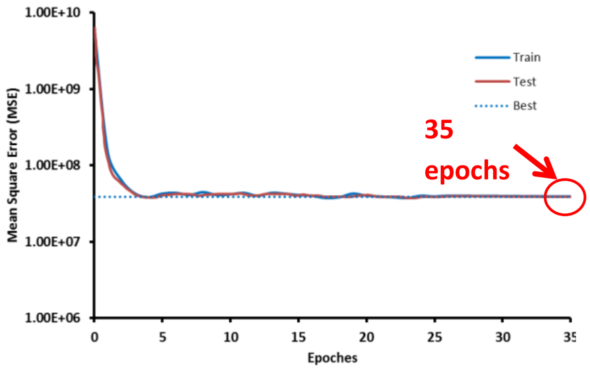

Figure 12: The network performance in terms of MSE vs. the number of epochs

The regression plots for the training and test datasets are shown in Figure 13, where both exhibit R-values exceeding 0.985.

Four criteria are used to evaluate the accuracy of the final ANN model's prediction of force-time curves obtained under impact after training. These criteria, three of which are based on reference [36] and one based on the present work, are defined as follows: 1) The peak force error (PLE), 2) the mean force error throughout the whole impact process (MFE), 3) the absorbed energy error (AEE), and 4) the shortening error (ShE). By the peak force of the curves from the test set, PF_t, and the corresponding ANN prediction, $\mathrm{PF}_{\mathrm{ANNN}}$, the PFE is defined as [36]:

$$\mathrm{PFE} = \frac{|\mathrm{PF}_{\mathrm{ANN}} - \mathrm{PF}_{\mathrm{t}}|}{\mathrm{PF}_{\mathrm{t}}} \tag{12}$$

Four criteria are used to evaluate the accuracy of the final ANN model's prediction of force-time curves obtained under impact after training. These criteria, three of which are based on reference [36] and one based on the present work, are defined as follows: 1) The peak force error (PLE), 2) the mean force error throughout the whole impact process (MFE), 3) the absorbed energy error (AEE), and 4) the shortening error (ShE). By the peak force of the curves from the test set, {PF}_t, and the corresponding ANN prediction, {\rm PF}_{ANN}N, the PFE is defined as [36]:

$$\mathrm{PFE} = \frac{|\mathrm{PF}_{\mathrm{ANN}} - \mathrm{PF}_{\mathrm{t}}|}{\mathrm{PF}_{\mathrm{t}}} \tag{12}$$

[DOI: 10.22068/ase.2026.745]

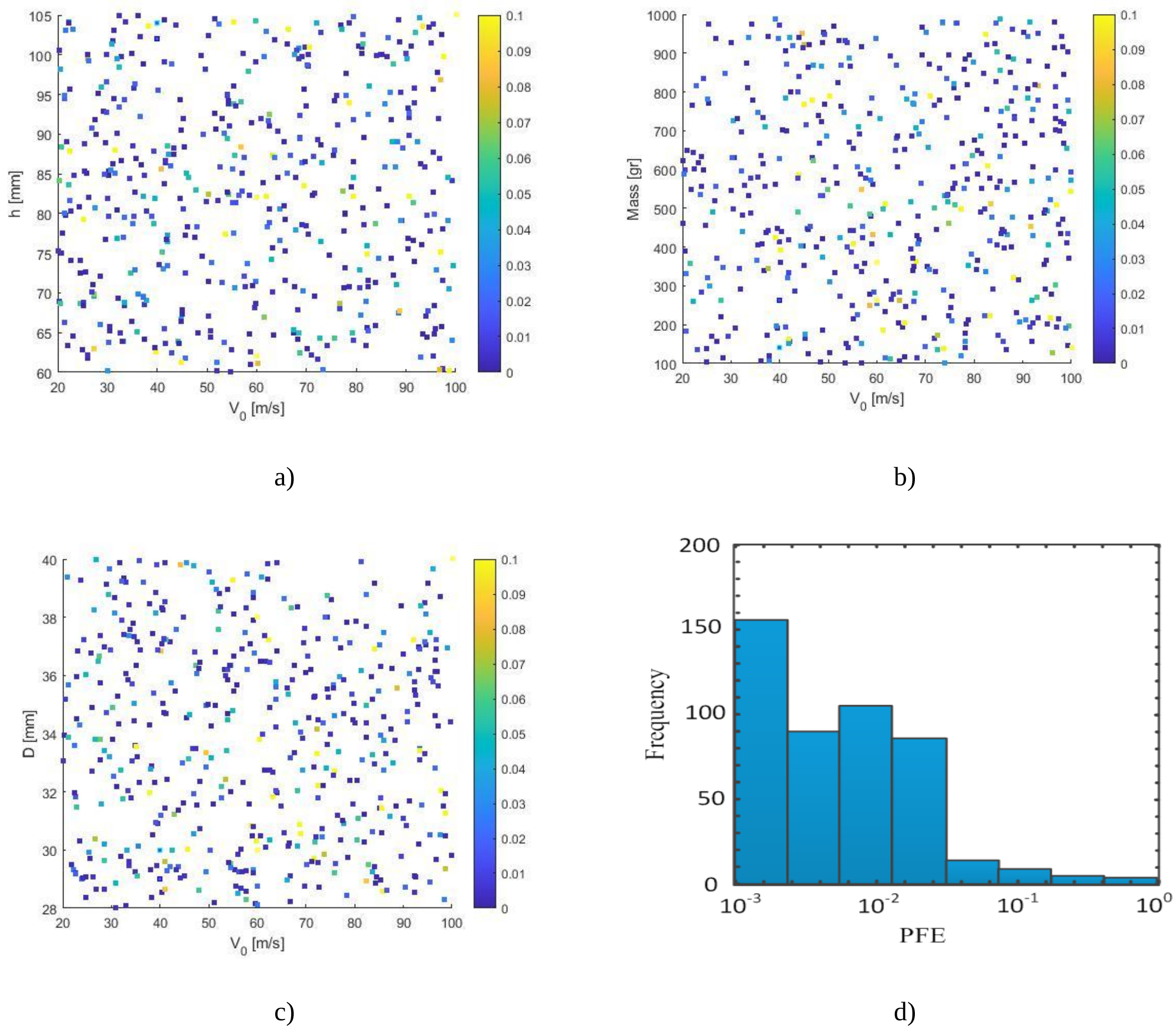

Figure 14: Distribution of the PFE on the test set in terms of (a) high vs velocity, (b) Striker Mass vs velocity, (c) diameter vs velocity and (d) histogram of the distribution of PFE on the test set.

The peak force occurs at the start of the crushing process and corresponds to the formation of the first plastic hinges. Given the abrupt variations in force observed at the onset of the impact process, the PFE criterion demonstrates the ANN model's ability to capture and accurately predict these rapid fluctuations. Figure 14a to figure 14c and figure 14d indicate the distribution and histogram of the PFE criterion on the test set, respectively.

According to our findings, the ANN model offers high accuracy in prediction of peak forces, with an average prediction error of less than 10% (figure 14d). Considering the number of input variables and their influence on the response, the distributions of predictions with respect to variations in height of tube, striker mass, and diameter of tube relative to striker velocity are illustrated in figures 14a, 14b, and 14c, respectively. These distributions reveal a non-uniform pattern in responses to the PFE predictions in the test set.

The second criterion, the mean force error, is defined as [36]

[DOI: 10.22068/ase.2026.745]

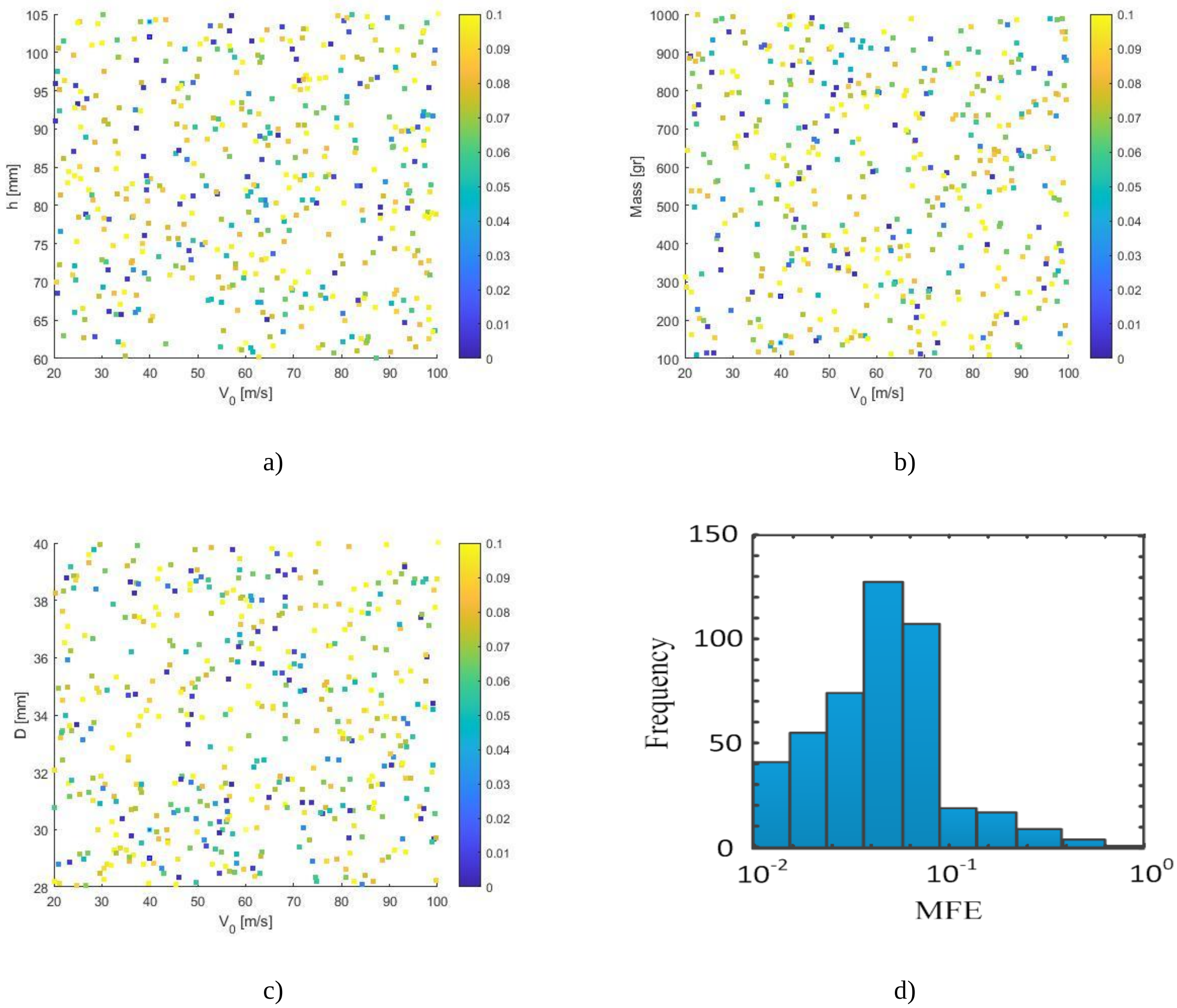

Figure 15: Distribution of the MFE on the test set in terms of (a) high of tube vs velocity, (b) Striker Mass vs velocity, (c) diameter of tube vs velocity and (d) histogram of the distribution of MFE on the test set.

$$MFE = \frac{\sum|\mathrm{MF_{ANN}} - \mathrm{MF}_t|}{\sum \mathrm{MF}_t} \quad (13)$$

Where $\mathrm{MF_{ANN}}$ represents the mean force obtained from the ANN model predictions and MF_t is the mean force of the curves from the test dataset. The MFE essentially represents the primary metric used for network optimization during training [36]. Figure 15a-15c and fgure 165d show the distribution and histogram of the MFE criterion on the test set, respectively.

Since the mean force error (MFE) is computed as the cumulative deviation over the entire force-time response, its value being higher than that of the peak force error is not unexpected. However, the MFE provides a more comprehensive and reliable measure of model accuracy, as it can capture a wider range of prediction discrepancies produced by the ANN. Despite the inherent noise in impact behavior, only a limited number of predictions exhibit errors exceeding 10%. Nevertheless, the majority of MFE values remain below 10%.

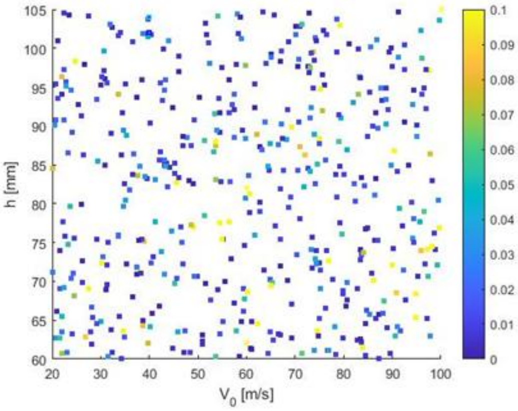

a)

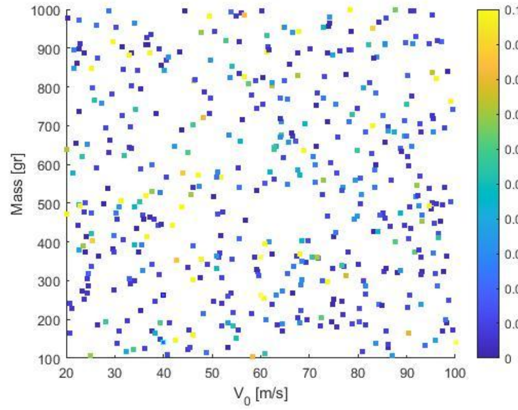

b)

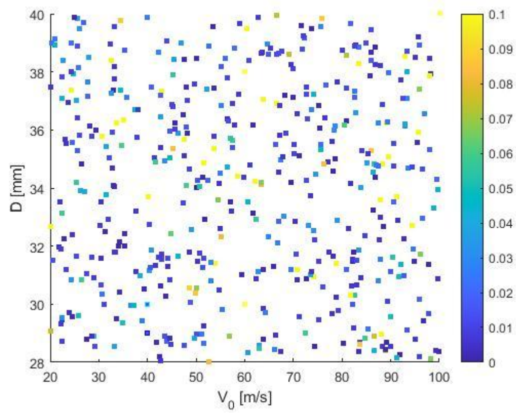

c)

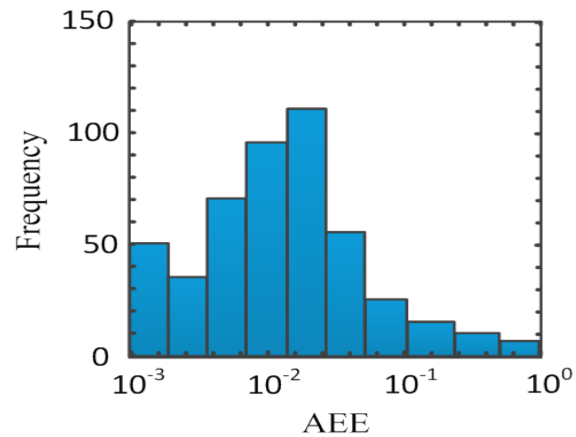

d)

Figure 16: Distribution of the AEE on the test set in terms of (a) high of tube vs velocity, (b) Striker Mass vs velocity, (c) diameter of tube vs velocity and (d) histogram of the distribution of AEE on the test set.

The relative error corresponding to the total absorbed energy is defined as [36]:

$$\mathrm{AEE} = \frac{|(\sum \mathrm{F_{ANN}}(\mathrm{t}))^2 - (\sum \mathrm{F_t}(\mathrm{t}))^2|}{(\sum \mathrm{F_t}(\mathrm{t}))^2} \qquad (14)$$

Where F_{ANN} represents the force obtained from the ANN model predictions and F_t denotes the force of the curves from the test dataset, and the sum symbol in Eq. (8) denotes the sum performed in the complete force–time response. Figure 16a-16c and figure 16d exhibit the distribution and histogram of the AEE criterion on the test set, respectively.

As the total absorbed energy represents an integral quantity, the Absorbed Energy Error (AEE) is significantly lower than the mean force error (MFE). Most of the predicted curves exhibit errors below 10%, with a considerable portion showing deviations of less than 0.1%. However, a few instances still display relatively large errors, in some cases exceeding 100%.

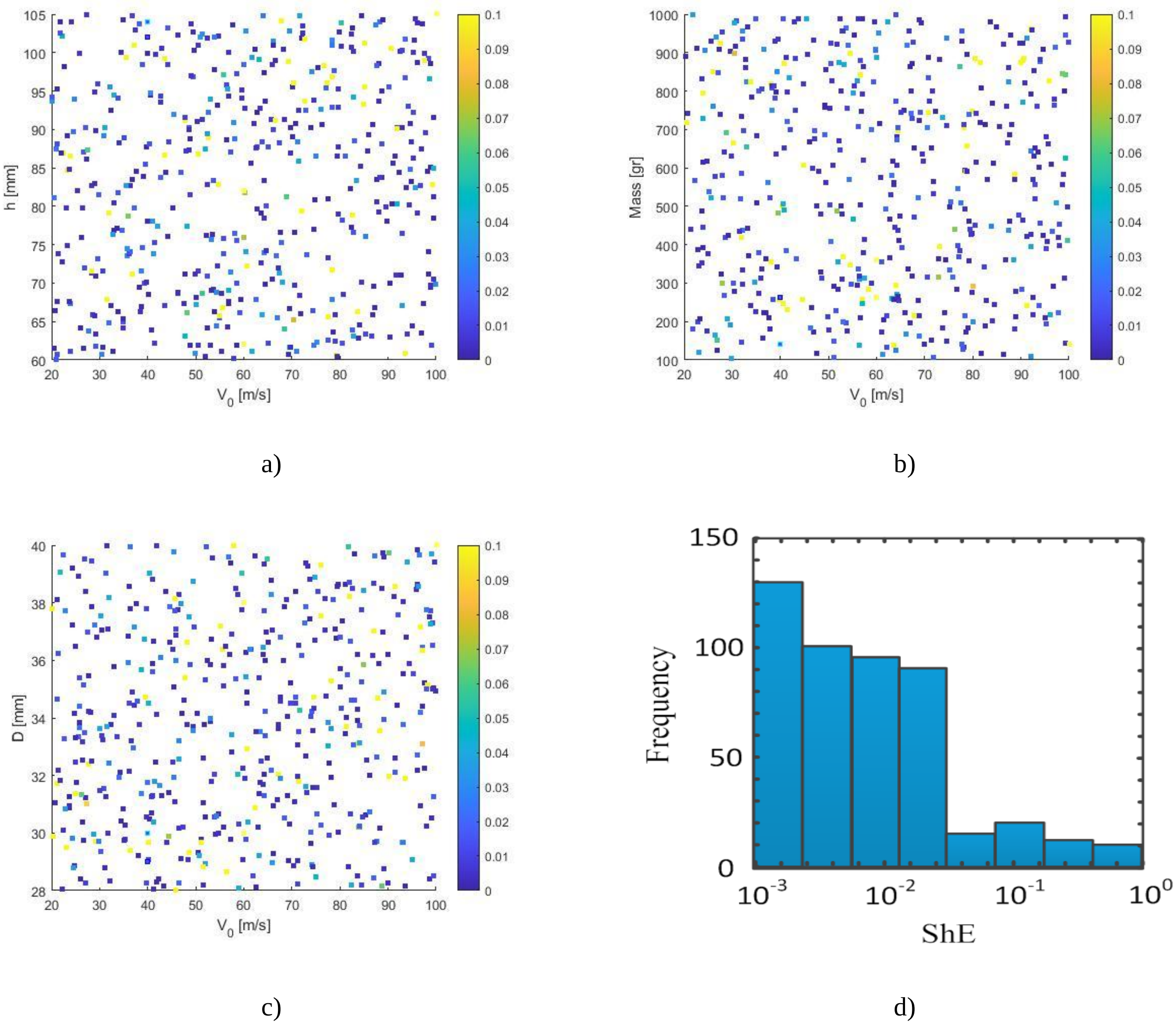

Figure 17: Distribution of the ShE on the test set in terms of (a) high of tube vs velocity, (b) Striker Mass vs velocity, (c) diameter of tube vs velocity and (d) histogram of the distribution of ShE on the test set.

Moreover, the distributions of MFE and AEE reveal similar trends, characterized by an escalation in both criteria at lower heights for tubes and higher impact velocities.

The last criterion, the shortening error, is defined as

$$ShE = \frac{|\mathrm{Sh_{ANN}} - \mathrm{Sh_t}|}{\mathrm{Sh_t}} \tag{15}$$

Where Sh_{ANN} represents the shortening obtained from the ANN model predictions and Sh_t denotes the shortening from the test dataset. Figure 17a to figure 17c and figure 17d indicate the distribution and histogram of the ShE criterion on the test set, respectively.

The shortening is measured upon completion of the crushing process and represents the tube's final deformation resulting from the impact. As shortening is directly associated with the duration of the impact event, the Shortening Error (ShE) metric reflects the ANN model's

[DOI: 10.22068/ase.2026.745]

ability to accurately capture and predict the temporal evolution of the deformation process.

As shown by the results, the ANN model achieves high accuracy in predicting shortening, with an average prediction error of less than 10% (Fig. 18d). In some cases, errors exceeding 10% are also observed, particularly at higher impact velocities or greater tube lengths.

Overall, the ANN model's predictions on the test dataset show satisfactory accuracy, though some cases exhibit notable errors.

4.3. Comparison of ANN model results with numerical and experimental results

To evaluate the ANN model's performance, its predictions are compared with both numerical simulations and experimental results. Two samples (i.e., T3 and T20) are selected from the test dataset for this purpose. The force-time curves predicted by the ANN model are compared with the corresponding experimental and simulation results for these samples.

Figure 18 presents the location of these two samples on the PFE distribution diagram, plotted as a function of impact velocity and tube height.

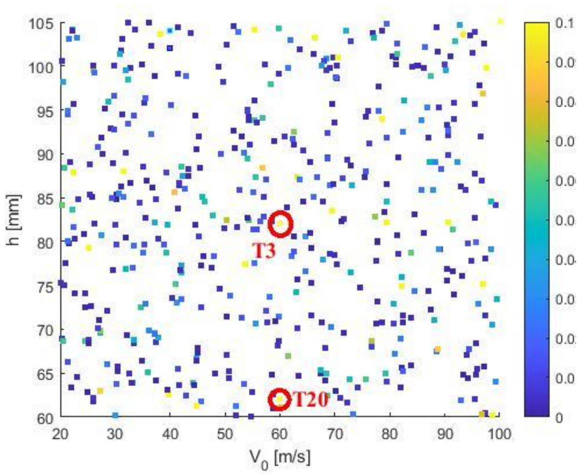

Figure 18: T3 and T20 superimposed on top of the distribution of the peak force error on the test set.

Figure 19a and 19b compare the force-time curves predicted by the ANN model with the corresponding experimental and numerical results for samples T3 and T20, respectively.

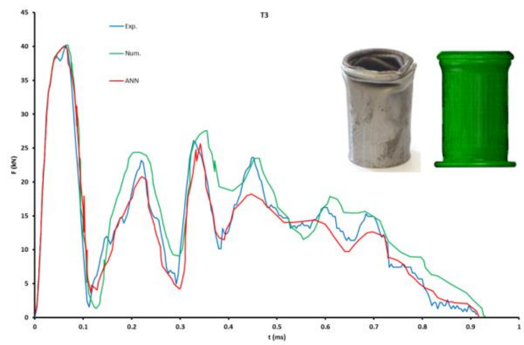

a)

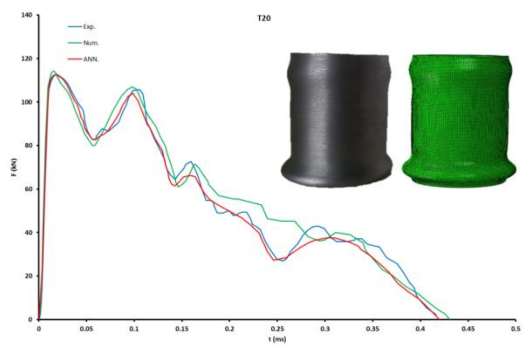

b)

Figure 19: Compare the force–time curves predicted by the ANN model with the corresponding experimental and numerical results for samples (a) T3 and (b) T20 on the test set.

In both curves, all the oscillations in the force-time curve are very close to the predictions of the finite element models and the experimental behavior. Although the ANN predictions exhibit a total average effect, some oscillations differ from the experimental model. However, when experimental curves are used alongside simulation during ANN training, the model performs better than the numerical simulation in some oscillations. The ANN model is also precise in forecasting the process time and the crushing stopping point. In general, the ANN model's predictions show better agreement with the experimental results than with the numerical simulation, indicating its accuracy.

[DOI: 10.22068/ase.2026.745]

5. Conclusions

1. The experimental and numerical datasets comprising 300 impact tests and 4,000 FE simulations provide a robust and comprehensive basis for training the ANN model, effectively capturing the influence of geometric and loading variations on force-time response.

2. The FE simulations demonstrate high consistency with experimental results in terms of force–time behavior, peak force, displacement, and buckling shape, confirming their reliability for generating training data for the ANN model.

3. Systematic evaluation of ANN architectures reveals that network depth and neuron density significantly influence prediction accuracy, with diminishing returns observed beyond approximately 20-26 hidden layers.

4. The optimized ANN architecture, consisting of 24 hidden layers with 180 neurons per layer and ReLU activation, achieves the best balance between accuracy and computational cost.

5. The trained ANN achieves strong predictive performance, with R-values exceeding 0.985 for both training and testing datasets, indicating high correlation between predicted and true force-time responses.

6. Error assessments across four physical criteria (PFE, MFE, AEE, and ShE) show that the ANN model predicts peak force, mean force, absorbed energy, and shortening with average errors generally below 10%, demonstrating strong predictive capability.

7. Despite the inherent noise and nonlinear oscillations in impact behavior, the ANN model is capable of accurately capturing the key dynamic features of the force-time curve. However, slight smoothing effects appear in high-frequency fluctuations.

8. The ANN model exhibits significant computational efficiency, predicting force-time curves more than 10,000× faster than explicit FE simulations and making it highly suitable for large-scale parametric studies and rapid design evaluations.

9. Comparison with experimental and numerical responses for representative samples (T3 and T20) confirms that the ANN can accurately reproduce oscillatory behavior, process duration, and crushing termination, often matching or outperforming FE predictions in localized oscillations.

10. Overall, the developed ANN model proves to be a reliable, efficient, and accurate tool for predicting crashworthiness and impact response of thin-walled cylindrical tubes, demonstrating strong potential for integration into design optimization frameworks and real-time engineering applications.

Declaration of Conflicting Interests

The author(s) declared no potential conflicts of interest with respect to the research, authorship, and/or publication of this article.

References

[1] R.D. Hussein, D. Ruan, G. Lu, S. Guillow, J.W. Yoon, Crushing response of square aluminium tubes filled with polyurethane foam and aluminium honeycomb, Thin-Walled Structures 110 (2017) 140-154.

[2] H. Sun, C. Ge, Q. Gao, N. Qiu, L. Wang, Crashworthiness of sandwich cylinder filled with double-arrowed auxetic structures under axial impact loading, International Journal of Crashworthiness 27(5) (2022) 1383-1392.

[3] A.A. Nia, J.H. Hamedani, Comparative analysis of energy absorption and deformations of thin walled tubes with various section geometries, Thin-Walled Structures 48(12) (2010) 946-954.

[4] C. Nagaraj, A.P. Kumar, M.G. Rao, L.P. Sankar, Numerical analysis on the deformation behavior of cylindrical tubes with end-capped shells under axial impact, Materials Today: Proceedings 27 (2020) 1917-1922.

[5] W. Abramowicz, Thin-walled structures as impact energy absorbers, Thin-walled structures 41(2-3) (2003) 91-107.

[DOI: 10.22068/ase.2026.745]

[6] D. Karagiozova, N. Jones, Influence of stress waves on the dynamic progressive and dynamic plastic buckling of cylindrical shells, International Journal of Solids and Structures 38(38-39) (2001) 6723-6749.

[7] H. Han, J. Cheng, F. Taheri, N. Pegg, Numerical and experimental investigations of the response of aluminum cylinders with a cutout subject to axial compression, Thin-Walled Structures 44(2) (2006) 254-270.

[8] Y. Tai, M. Huang, H. Hu, Axial compression and energy absorption characteristics of high-strength thin-walled cylinders under impact load, Theoretical and applied fracture mechanics 53(1) (2010) 1-8.

[9] R. Rajabiehfard, A. Darvizeh, M. Darvizeh, R. Ansari, M. Alitavoli, H. Sadeghi, Theoretical and experimental analysis of elastic–plastic cylindrical shells under two types of axial impacts, Thin-Walled Structures 107 (2016) 315-326.

[10] R. Rajabiehfard, A. Darvizeh, M. Alitavoli, R. Ansari, E. Maghdouri, Experimental, numerical and analytical investigations into the internal inversion of mild steel tubes under high velocity axial impact using a die, Thin-Walled Structures 125 (2018) 21-37.

[11] M.M. Abadi, A. Alijani, S.G. Rad, M. Salehpour, High-velocity impact response of cylindrical tubes with linear gradient grooves: A comparative study, Thin-Walled Structures 179 (2022) 109741.

[12] S. Bhutada, M.D. Goel, Progressive axial crushing behaviour of Al6061-T6 alloy tubes with geometrical modifications under impact loading, Thin-Walled Structures 182 (2023) 110240.

[13] F. Raoof, J. Rezapour, S. Gohari Rad, R. Rajabiehfard, Comparative Analysis of Crashworthiness of Empty and Hybrid Mild Steel-High Density Polyethylene Cylindrical Tubes Under High Axial Impact, Journal of Dynamic Behavior of Materials 9(1) (2023) 106-123.

[14] Z. Fan, G. Lu, K. Liu, Quasi-static axial compression of thin-walled tubes with different cross-sectional shapes, Engineering Structures 55 (2013) 80-89.

[15] Z. Liu, W. Hao, J. Xie, J. Lu, R. Huang, Z. Wang, Axial-impact buckling modes and energy absorption properties of thin-walled corrugated tubes with sinusoidal patterns, Thin-Walled Structures 94 (2015) 410-423.

[16] J. Ma, Z. You, Energy absorption of thin-walled square tubes with a prefolded origami pattern—part I: geometry and numerical simulation, Journal of applied mechanics 81(1) (2014).

[17] M. Koloushani, M.R. Forouzan, M.R. Niroomand, On the crashworthiness performance of thin-walled circular tubes: Effect of diameter and thickness, Mechanics of Advanced Materials and Structures (2023) 1-13.

[18] L. Teng, D. Qingtian, L. Xinbo, Energy absorption and deformation modes of several thin-walled tubes under dynamic compression, Structures, Elsevier, 2023, pp. 890-897.

[19] D. Karagiozova, N. Jones, Dynamic elastic–plastic buckling of circular cylindrical shells under axial impact, International Journal of solids and Structures 37(14) (2000) 2005-2034.

[20] X. Xu, Y. Ma, C. Lim, H. Chu, Dynamic buckling of cylindrical shells subject to an axial impact in a symplectic system, International Journal of Solids and Structures 43(13) (2006) 3905-3919.

[21] K. Yamazaki, J. Han, Maximization of the crushing energy absorption of cylindrical shells, Advances in Engineering Software 31(6) (2000) 425-434.

[22] H. Sadeghi, M. Alitavoli, A. Darvizeh, R. Rajabiehfard, Dynamic plastic behaviour of

[DOI: 10.22068/ase.2026.745]

strain rate sensitive tubes under axial impact, Thin-Walled Structures 143 (2019) 106220.

[23] J. Sun, X. Xu, C.W. Lim, Localization of dynamic buckling patterns of cylindrical shells under axial impact, International Journal of Mechanical Sciences 66 (2013) 101-108.

[24] S. Yao, Y. Huo, K. Yan, P. Xu, Crashworthiness study on circular hybrid corrugated tubes under axial impacts, Thin-Walled Structures 145 (2019) 106358.

[25] M. Ferdynus, M. Kotełko, M. Urbaniak, Crashworthiness performance of thin-walled prismatic tubes with corner dents under axial impact-Numerical and experimental study, Thin-Walled Structures 144 (2019) 106239.

[26] S. Feli, E. Makhsousse, S.S. Jafari, Dynamic progressive buckling of thin-wall grooved conical tubes under impact loading, International Journal of Crashworthiness 25(2) (2020) 220-229.

[27] M. Jamal-Omidi, A. Choopanian Benis, A numerical study on energy absorption capability of lateral corrugated composite tube under axial crushing, International journal of crashworthiness 26(2) (2021) 147-158.

[28] B. Lu, C. Shen, J. Zhang, D. Zheng, Z. Li, Energy absorption analysis of square-circle hybrid section tubes under axial loading, International Journal of Crashworthiness 27(3) (2022) 800-815.

[29] Khalkhali A, Afroosheh M, Seyedi M. Modeling and prediction of FRP composite cylinder tubes crashworthiness characteristics. Automotive Science and Engineering, Vol.1, No. 4, (2014), pp. 664-674.

[30] S. Bhutada, M. Goel, Crashworthiness parameters and their improvement using tubes as an energy absorbing structure: an overview, International Journal of Crashworthiness 27(6) (2022) 1569-1600.

[31] R. Guarize, N. Matos, L. Sagrilo, E. Lima, Neural networks in the dynamic response analysis of slender marine structures, Applied Ocean Research 29(4) (2007) 191-198.

[32] P. Mandal, Artificial neural network prediction of buckling load of thin cylindrical shells under axial compression, Engineering Structures 152 (2017) 843-855.

[33] A.A. Dastjerdi, H. Shahsavari, A. Eyvazian, F. Tarlochan, Crushing analysis and multi-objective optimization of different length bi-thin walled cylindrical structures under axial impact loading, Engineering Optimization 51(11) (2019) 1884-1901.

[34] T. Chen, Y. Zhang, J. Lin, Y. Lu, Theoretical analysis and crashworthiness optimization of hybrid multi-cell structures, Thin-Walled Structures 142 (2019) 116-131.

[35] P. Mandal, M.T. Adil, F. Naz, Application of artificial neural network to predict buckling load of thin cylindrical shells under axial compression, Engineering Structures 248 (2021) 113221.

[36] E. Sakaridis, N. Karathanasopoulos, D. Mohr, Machine-learning based prediction of crash response of tubular structures, International Journal of Impact Engineering 166 (2022) 104240.

[37] D. Wang, P. Xu, C. Yang, X. Xiao, Q. Che, Crashing performance and multi-objective optimization of honeycomb-filled thin-walled energy absorber with axisymmetric thickness, Mechanics of Advanced Materials and Structures (2022) 1-18.

[38] Raoof F, Rezapour J, Gohari Rad S, Rajabiehfard R. Investigating the density of Polyurethane foam on crashworthiness and energy absorption parameters in foam filled tubes under axial quasi-static loading. ASE 2023; 13 (2) :4110-4118

[39] H. Sadeghi, K. Davey, R. Darvizeh, R. Rajabiehfard, A. Darvizeh, An investigation into

[DOI: 10.22068/ase.2026.745]

finite similitude for high-rate loading processes: advantages in comparison to dimensional analysis and its practical implementation, International Journal of Impact Engineering 140 (2020) 103554.

[40] X. Lu, D.G. Giovanis, J. Yvonnet, V. Papadopoulos, F. Detrez, J. Bai, A data-driven computational homogenization method based on neural networks for the nonlinear anisotropic electrical response of graphene/polymer nanocomposites, Computational Mechanics 64 (2019) 307-321.

[41] Y. Wang, Q. Zeng, J. Wang, Y. Li, D. Fang, Inverse design of shell-based mechanical metamaterial with customized loading curves based on machine learning and genetic algorithm, Computer Methods in Applied Mechanics and Engineering 401 (2022) 115571.